Why Do Similar Patterns of Tropical Convection Yield Extratropical Circulation Anomalies of Opposite Sign?

MICHAEL GOSS AND STEVEN B. FELDSTEIN

Department of Meteorology, The Pennsylvania State University, University Park, Pennsylvania

(Manuscript received 26 February 2016, in final form 6 September 2016)

ABSTRACT

Tropical precipitation anomalies associated with El Niño and Madden–Julian oscillation (MJO) phase 1 (La Niña and MJO phase 5) are characterized by a tripole, with positive (negative) centers over the Indian Ocean and central Pacific and a negative (positive) center over the warm pool region. However, their midlatitude circulation responses over the North Pacific and North America tend to be of opposite sign. To investigate these differences in the extratropical response to tropical convection, the dynamical core of a climate model is used, with boreal winter climatology as the initial flow. The model is run using the full heating field for the above four cases, and with heating restricted to each of seven small domains located near or over the equator, to investigate which convective anomalies may be responsible for the different extratropical responses. An analogous observational study is also performed. For both studies, it is found that, despite having a similar tropical convective anomaly spatial pattern, the extratropical response to El Niño and MJO phase 1 (La Niña and MJO phase 5) is quite different. Most notably, responses with opposite-signed upper-tropospheric geopotential height anomalies are found over the eastern North Pacific, northwestern North America, and the southeastern United States. The extratropical response for each convective case most closely resembles that for the domain associated with the largest-amplitude precipitation anomaly: the central equatorial Pacific for El Niño and La Niña and the warm pool region for MJO phases 1 and 5.

1. Introduction

Large-scale complexes of tropical convective storms, initiated in part by warm sea surface temperature (SST) anomalies over the equatorial oceans, can alter large-scale weather patterns in the extratropics (Bjerknes 1966, 1969; Rowntree 1972; Shukla and Wallace 1983; Lau and Phillips 1986; Trenberth et al. 1998). The extratropical response to tropical convection is a Rossby wave train, which has its source in the interaction between the divergent flow associated with the latent heat released by the convective complexes and the absolute vorticity in the subtropics: that is, the so-called Rossby wave source (Sardeshmukh and Hoskins 1988; Qin and Robinson 1993). The location and amplitude of this extratropical wave train response is therefore intricately tied to the location and amplitude of the convective anomalies near the equator (Geisler et al. 1985; Kiladis and Weickmann 1992; Lin and Derome 2004), as well as the state of the extratropical initial flow (Ting and Sardeshmukh 1993; Goss and Feldstein 2015). Two important phenomena that are associated with tropical convection are the El Niño–Southern Oscillation (ENSO), which varies on the seasonal time scale, and the Madden–Julian oscillation (MJO), which propagates eastward with a period of 30–60 days. Typically, ENSO is separated into three phases—El Niño, neutral, and La Niña—often based upon the SST in the Niño-3.4 region (defined as the SST in a box located between 5°S and 5°N and between 170° and 120°W), and the MJO is divided into eight phases that describe the longitude of the large-scale outgoing longwave radiation (OLR) and 200- and 850-hPa zonal wind anomalies in the tropics (Wheeler and Hendon 2004). Many previous studies have found a large sensitivity of the extratropical response to the phase of both ENSO and the MJO, as will be discussed below.

Convective heating associated with the MJO in phases 1 and 5, and the El Niño and La Niña phases of ENSO, is characterized on large scales by a tripole anomaly in both the precipitation and OLR fields, with anomalies of one sign being located over the equatorial central Pacific and Indian Oceans and an anomaly of the opposite sign located over the Maritime Continent. Specifically, MJO

Corresponding author e-mail: Michael Goss, mag475@psu.edu

DOI: 10.1175/JAS-D-16-0067.1

phase 1 and El Niño are both associated with enhanced convection (anomalously negative OLR) over the central Pacific and Indian Oceans and suppressed convection (anomalously positive OLR) over the Maritime Continent. Opposite-signed anomalies are seen in the MJO phase 5 and La Niña cases (Wheeler and Hendon 2004; also see Rasmusson and Carpenter 1982). Importantly, the amplitudes of these maxima differ substantially, with the ENSO cases showing the strongest-amplitude convective signal over the central Pacific and the MJO cases showing the strongest-amplitude convective signal over the Maritime Continent. For El Niño, these convective anomalies are also coupled to SST anomalies, with anomalously warm SSTs found over the equatorial central Pacific and Indian Oceans and anomalously cool SSTs located near the Maritime Continent, with opposite-signed anomalies for La Niña.

Interestingly, even though the MJO phase 1 and El Niño OLR (as well as the MJO phase 5 and La Niña) patterns resemble each other, as discussed above, the extratropical response to MJO phase 1 does not resemble the extratropical response to El Niño, and, likewise, the extratropical response to MJO phase 5 does not resemble that associated with La Niña. Specifically, the extratropical response to MJO phase 1 (phase 5) projects onto the negative (positive) phase of the Pacific–North America (PNA) teleconnection pattern (Mori and Watanabe 2008; Johnson and Feldstein 2010; Moore et al. 2010; Franzke et al. 2011; Yoo et al. 2012; Riddle et al. 2013). On the other hand, the extratropical response to El Niño (La Niña) projects onto the positive (negative) phase of the PNA (e.g., Horel and Wallace 1981; Wallace and Gutzler 1981; Trenberth et al. 1998; Johnson and Feldstein 2010). Therefore, while the large-scale El Niño and MJO phase 1 (La Niña and MJO phase 5) equatorial convective anomalies show a similar spatial structure, the responses over the extratropics tend to be associated with circulation anomalies of opposite sign.

Therefore, given the issues raised above, we aim to address the following major questions in this study: 1) Does a simple global dynamical model successfully reproduce the main differences in the extratropical response to MJO phase 1 convective heating and El Niño convective heating (MJO phase 5 convective heating and La Niña convective heating)? 2) Do there appear to be particular convective regions in the model that are responsible for the largest contribution to the extratropical response to the ENSO and MJO convective heating? 3) If so, can differences in the key convective regions explain the differences in the modeled extratropical responses to ENSO and MJO convective heating? 4) Are the model results with respect to Q2 and Q3 consistent with observations?

In section 2 of this paper, we discuss the data and methods used to carry out the study. Section 3 presents the results of the model experiments. Section 4 shows observational results analogous to the model results in section 3. Finally, in section 5, the conclusions are presented.

2. Methods and data

In this study, we use the dynamical core of a National Oceanic and Atmospheric Administration/Geophysical Fluid Dynamics Laboratory (NOAA/GFDL) climate model. The model is run with triangular 42 horizontal resolution and 19 vertical levels in sigma coordinates. The model is forced by radiative relaxation. Rayleigh friction is applied for $\sigma > 0.7$, with a 1-day damping time scale at the surface that increases with height as in Held and Suarez (1994). No Rayleigh friction is applied for $\sigma \leq 0.7$. Fourth-order horizontal diffusion is included with a time scale of 0.1 days at the smallest resolvable scale, and we run the model without vertical diffusion. Newtonian cooling is applied to the perturbation temperature, where a perturbation refers to the deviation from the model's initial state, which corresponds to the observed December–February (DJF) climatology for the years 1979–2012, calculated as the mean of the daily fields of the European Centre for Medium-Range Weather Forecasts interim reanalysis (ERA-Interim) dataset (Dee et al. 2011). Since the climatology does not result in a balanced state in the model, the model equations are supplemented with a constant forcing term, which exactly balances the model drift when integrating the equations forward in time from the climatological state.

In the model runs, various heating fields are added to the above initial flow. The heating in the model is stationary[1] and is active from day 0 through day 10. Separate heating fields are specified for El Niño, La Niña, and MJO phases 1 and 5. The horizontal structure of the heating fields for the model runs are derived from composites of a daily interpolation of NOAA's Climate Prediction Center (CPC) Merged Analysis of

[1] To test the sensitivity of the modeled response to a moving versus a stationary heating source, we additionally performed analogous model calculations in which the heating field was changed daily in a manner consistent with a 48-day MJO cycle. All of the heating fields were still derived from precipitation composites. We found that, although the spatial pattern was slightly altered and the amplitude increased in the moving convection case, the key findings of the study were unchanged.

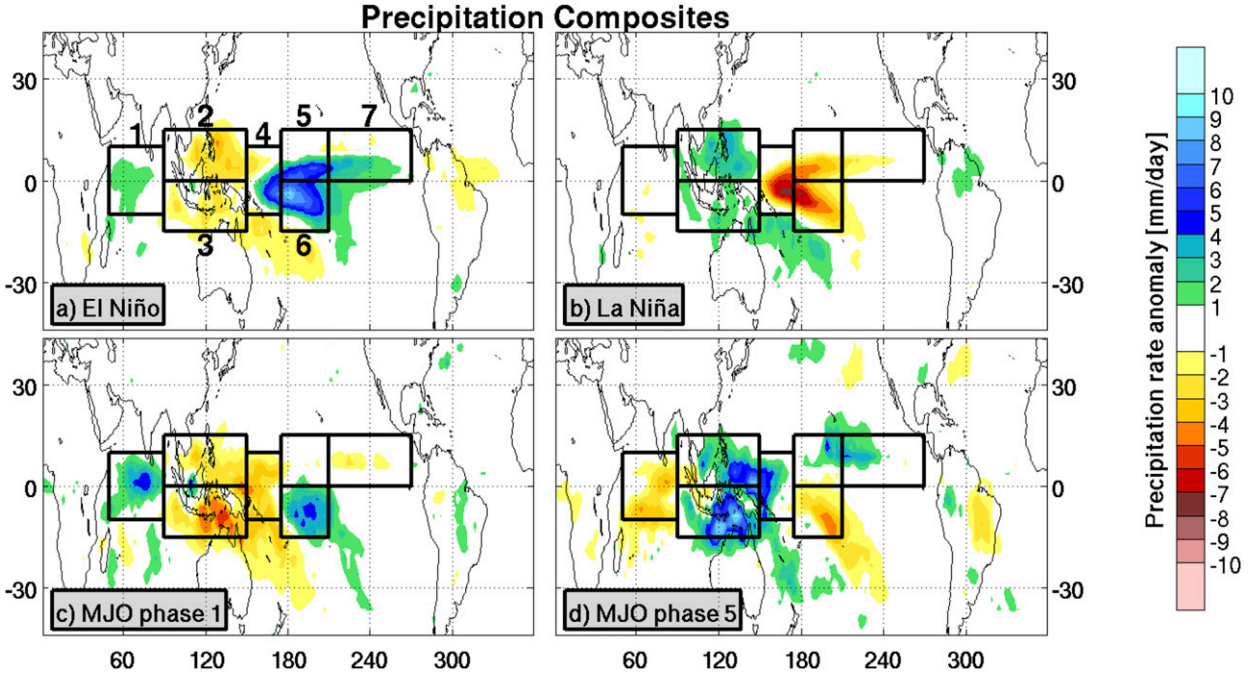

FIG. 1. Precipitation composites for (a) El Niño days, (b) La Niña days, (c) MJO phase 1 days, and (d) MJO phase 5 days (see text for details). Seven domains (labeled 1–7 in the El Niño plot) are outlined with black rectangles.

Precipitation data (CMAP; Xie and Arkin 1997).[2] The precipitation rate is converted to a heating rate by multiplying the precipitation rate by the latent heat of vaporization of water and the density of water, then dividing by the heat capacity of water at constant pressure. The vertical structure is specified as in Yoo et al. (2012), where the maximum heating anomaly is at the $\sigma = 0.5$ level. For El Niño, all days in DJF months that are classified as El Niño months are included in the precipitation composite, and an analogous composite is calculated for La Niña months (Figs. 1a,b). The definition of El Niño and La Niña months is adapted from that used by the CPC. Those months when the Oceanic Niño Index, which is defined as the 3-month running-mean SST anomaly in the Niño-3.4 region, is greater than or equal to 0.5 (less than or equal to −0.5) for at least five consecutive months, are considered to be El Niño (La Niña) months. The MJO phases are based on the multivariate MJO index of Wheeler and Hendon (2004). Briefly, we use the real-time multivariate MJO (RMM) indices from that study, where the RMM1 and RMM2 indices are the principal component time series of the first two combined empirical orthogonal functions of 200- and 850-hPa zonal wind and OLR in the tropics, and the phase is determined by the relative values of the two indices. For the MJO phase 1 precipitation composite, we include those DJF days when the Wheeler and Hendon (2004) MJO index is in phase 1 with an amplitude greater than 1.0 (Fig. 1c). An analogous method is used to calculate the MJO phase 5 precipitation composite (Fig. 1d).

We will first compare the differences in the model's extratropical response to ENSO-like and MJO-like heating. We assume that the ENSO response, which is typically associated with much longer time scales, can be sufficiently captured by the model within the 10-day window over which the model is run. This assumption is supported by Hoskins and Karoly (1981), who find that the extratropical response to tropical convection typically occurs on a time scale of about 7–10 days. Then the ENSO and MJO precipitation composites will be separated into a grid of 7 smaller domains, as shown in Fig. 1. The domains used to test the response to localized convective anomalies are shown as boxes numbered 1–7.

[2] The sensitivity of our study to the precipitation source was also tested. In addition to the interpolated CMAP data, we ran all of our model analyses using the same methodology, but with precipitation data from the National Aeronautics and Space Administration's Tropical Rainfall Measuring Mission (TRMM; with data only going back to 1998) and from the research version of NOAA's Global Precipitation Climatology Project (GPCP). We found that the precipitation composites were almost identical, with the biggest differences being associated with some of the weaker precipitation anomalies over South America. The modeled responses showed minor differences, and the results and main conclusions of the study were not significantly altered by the choice of precipitation source.

Domain 1 is centered over the equatorial Indian Ocean, from 50° to 90°E and from 10°S to 10°N. Domains 2 and 3 are located north and south of the equator over the Maritime Continent, from 90° to 150°E and from the equator to 15°N and 15°S, respectively. Domain 4 is found west of the international date line over the equatorial Pacific, from 150° to 175°E and from 10°S to 10°N. Domains 5 and 6 are located north and south of the equator over the central equatorial Pacific, from 175°E to 150°W and from the equator to 15°N and 15°S, respectively. Finally, domain 7 is found along the intertropical convergence zone in the northeastern Pacific, from 150° to 90°W and from the equator to 15°N. These domains are chosen because they are regions over which the MJO and ENSO signals are either of the same sign (domains 1, 2, 3, and 6) or of opposites sign (domains 4, 5, and 7). In this way, we can determine the tropical convective regions that are responsible for the differences in the observed extratropical responses to ENSO and the MJO. Separate model runs are performed for each of the 7 model domains. Each model calculation is performed with a heating profile calculated from the composite precipitation anomaly in that domain, and outside the domain the composite precipitation anomaly is set to 0. The extratropical response is analyzed based on the 0.3σ-level geopotential height anomalies averaged over model days 7–10.

In the observational study, composites of localized tropical precipitation and 300-hPa geopotential heights are found in the CMAP and ERA-Interim datasets by analogy with the model runs for individual domains. For these calculations, we use an analog method. A ''pattern'' to match, $P_{\text{pat}}(\lambda, \theta)$, is first found by using the precipitation field in Fig. 1 for each domain and then setting the precipitation to zero outside the domain. We then search for those days when the observed precipitation matches well with $P_{\text{pat}}(\lambda, \theta)$ for each of the seven domains in Fig. 1. To determine the analog days, we then calculate the root-mean-squared error [RMSE(t)] for each DJF day using

$$\text{RMSE}(t) = \frac{\sum_{i,j}\sqrt{[P_{\text{pat}}(\lambda,\theta) - P(t,\lambda,\theta)]^2}}{n_i n_j}. \quad (1)$$

Here, t corresponds to a DJF day; λ is the latitude; θ is the longitude; i and j correspond to the latitudinal and longitudinal grid points, respectively; n_i and n_j correspond to the number of latitudinal and longitudinal grid points, respectively; and P is the precipitation anomaly field for day t. The domain used for calculating RMSE(t) in (1) includes all grid points between 15°S and 15°N. The day with the lowest RMSE(t) value is the first analog day that is chosen, and that day is removed from the ''pool'' of analog days that are considered. An iterative method is then employed to determine the subsequent analog days, using

$$\text{RMSE}(d) = \frac{\sum_{i,j}\sqrt{[P_{\text{pat}}(\lambda,\theta) - P_{\text{comp}}(d,\lambda,\theta)]^2}}{n_i n_j}. \quad (2)$$

Here, d corresponds to the day from the remaining pool. The precipitation pattern for which analogs are being found is still P_{pat}, but P_{comp} is the analog-based precipitation composite that includes those days from the previous iterations in addition to day d. The day with the lowest RMSE(d) value is that which is chosen as the next analog day, and that day is then removed from the pool. In other words, at each step, the day chosen is that which minimizes the RMSE(d) value. The process is repeated until there are at least five consecutive iterations for which the RMSE value does not reach a new minimum, and the analog days that comprise the minimum RMSE value are those that are chosen for the precipitation composite for the corresponding domain and case. (The precipitation composites calculated in this manner are shown in the left column of Figs. 7–10 for each of the seven domains.) The number of analog days that result from this technique ranges from 127 to 1350. Finally, the corresponding lagged composites of the 300-hPa geopotential height anomalies averaged over lag days 7–10 for the analog days that contribute to the RMSE(d) value are calculated. These 300-hPa geopotential height composites are compared to the analogous model results.

Statistical significance of the observational results is tested by building distributions using Monte Carlo simulations, with 5000 simulations calculated for each significance test. Three types of Monte Carlo experiments are set up to test three different aspects of the observational analysis. In the first, we calculate pattern correlations between the observed El Niño (La Niña) and MJO phase 1 (MJO phase 5) precipitation composites over the domain 15°S–15°N, 50°E–90°W. We then generate 5000 pattern correlations between randomly generated precipitation composites over the same domain. For precipitation composites based on ENSO, we choose a number of random DJF seasons corresponding to the number of El Niño or La Niña seasons. For precipitation composites based on the MJO, we choose a number of random DJF days corresponding to the actual number of days in the MJO phase 1 or phase 5 composites, divided by the average number of consecutive days in the respective composites, in order to account for autocorrelation. The precipitation

pattern correlations associated with Fig. 1 are 0.5800 and 0.3876 for El Niño/MJO phase 1 and La Niña/MJO phase 5, respectively. The former value is statistically significant at the 99.92th percentile and the latter at the 96.06th percentile. This suggests a high degree of similarity between the composites.

A similar statistical test is performed to compare the observed 300-hPa geopotential height response to the full convective field (the total) with the sum of the observed 300-hPa geopotential height responses to the convective fields for each of the seven domains (the sum). Here, the pattern correlation is again calculated between the total and the sum response for each ENSO and MJO case for the domain ranging from 15° to 75°N and from 60°E to 60°W. Random geopotential height composites are calculated for each convective domain and for the full convective field, with the number of randomly selected DJF days corresponding to the number of analog days for the respective convective domain. The random sum is calculated using the sum of the randomly generated composites for each of the seven smaller convective domains, and the random total is simply the randomly generated composite corresponding to the full convective field. A pattern correlation is then calculated over the same spatial domain between the random total and sum composites, and this process is repeated 5000 times for each ENSO and MJO case, resulting in a distribution of 5000 random pattern correlations.

Finally, we test the significance of the response at each grid point in each of the analog-based observational 300-hPa geopotential height composites. For each case, we choose a number of random DJF days corresponding to the number of analogs for that case. Five thousand random composites are generated in this way for each case, and the value of the actual composite at each grid point is compared to the randomly generated distribution at the same grid point. Significance is tested at the $p < 0.05$ level.

3. Model results

We show the modeled days-7–10 anomalous 0.3σ geopotential height response to the imposed heating fields described above (top four panels of Fig. 2). For the El Niño case (Fig. 2a), we see anomalous highs over the tropical Pacific east of the international date line and over northwestern North America, with anomalous lows centered south of the Aleutian Islands, south of Greenland, and over the southeast United States. The La Niña response seen in Fig. 2b shows essentially the same spatial pattern, but with anomalies of opposite sign. Figure 2d shows the modeled response to MJO phase 5 forcing. An anomalous high can be seen over the tropical Pacific, with a maximum value to the west of the Hawaiian Islands, another high stretching from Kamchatka to the Aleutians and the southern coast of Alaska, and a third high centered over the northeastern United States and southeastern Canada. Anomalous lows are seen in a band between the two Pacific highs, with one maximum near Japan and Korea and a weaker maximum centered over the southwestern United States and northwestern Mexico. Finally, the response to MJO phase 1 forcing seen in Fig. 2c shows a similar spatial structure to that seen in Fig. 2d, but with anomalies of opposite sign. Notably, although the large-scale spatial structure of the El Niño and MJO phase 1 (La Niña and MJO phase 5) tropical convection composites are similar, as seen in Figs. 1a and 1c (Figs. 1b,d), the modeled extratropical responses shown in Figs. 2a and 2c (Figs. 2b,d) are quite different, especially over the Pacific and North America regions, where we see opposite-signed anomalies over the tropical North Pacific, the midlatitude North Pacific, northwestern North America, the southern United States and northern Mexico, and the northeastern United States and southeastern Canada.

For comparison, we also show the observed days-7–10 anomalous 300-hPa geopotential height response (bottom four panels of Fig. 2). Although the aim of this study is not to perfectly replicate the observed response in a simple dynamical core model, we do see many similarities, especially in the El Niño and La Niña cases. The MJO phase 1 response in the model resembles that in the observations except for the wave field appearing to be slightly compressed in the latitudinal direction. The MJO phase 5 response, like that of MJO phase 1, shows some similarities, with a somewhat more compressed wave field in the model compared to the observations, and with similarities most apparent over East Asia and the subtropical and the western North Pacific. Also, the amplitude of the response is about a factor of 3 smaller in the model than in the observations. We believe there are three main factors that account for this amplitude difference. First, the model is run from a climatological initial state, so high-frequency transient eddy feedback is largely absent from the simulations. Second, although the horizontal tropical heating field is based on the observed precipitation rate, the vertical structure of the heating is specified, and the amplitude of the extratropical response (not the spatial structure) in this model has been seen to be sensitive to the vertical structure of the tropical heating field (Yoo et al. 2012). Third, we performed the MJO model calculations using a moving heating source rather than a stationary heating source (see footnote 2 above), and found that the modeled

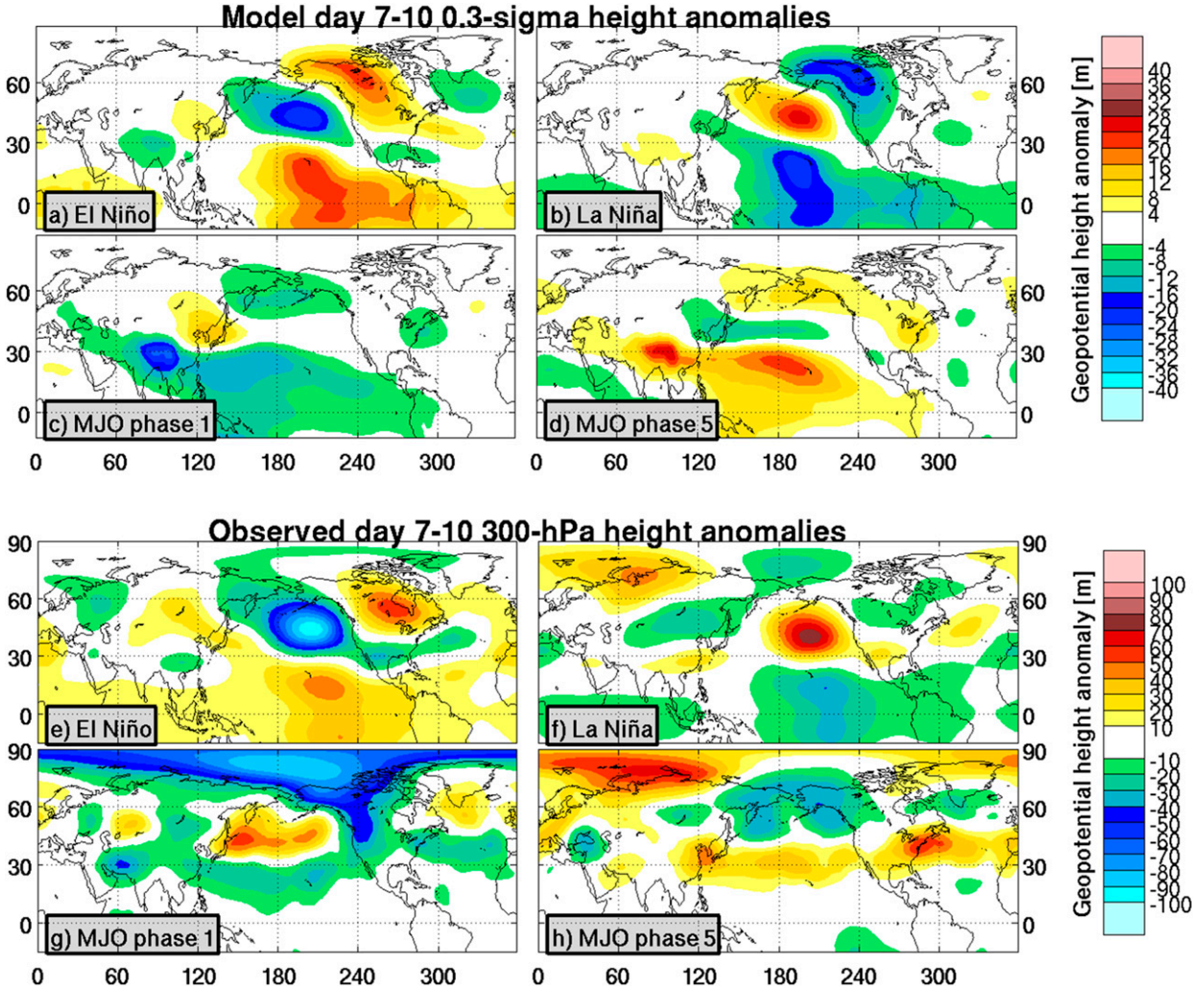

FIG. 2. (top) Days-7–10 0.3σ geopotential height anomalies for the model forced with heating based on (a) El Niño, (b) La Niña, (c) MJO phase 1, and (d) MJO phase 5. (bottom) Observed days-7–10 composite 300-hPa geopotential height anomalies for (e) El Niño, (f) La Niña, (g) MJO phase 1, and (h) MJO phase 5.

extratropical response shows a larger-amplitude signal, closer to the observations (not shown).

To further understand these different responses, we perform model calculations forced with heating limited to domains 1–7. In Figs. 3–6 , in the left column, we show the composite precipitation used to derive the model heating, and in the right column we see the resulting days-7–10 anomalous 0.3σ geopotential height response. [Note that enhanced (reduced) precipitation is shown with cold (warm) colors.] The third through the ninth rows in Figs. 3–6 correspond to the composite precipitation and the days-7–10 anomalous 0.3σ geopotential height fields for each of the domains 1–7, respectively. The second row is a simple sum of the precipitation and 0.3σ geopotential height for domains 1–7. For comparison, in the top row, we reproduce the precipitation and 0.3σ geopotential height fields shown in Figs. 1 and 2. We see that, for Figs. 3–6, the modeled response in the first row matches almost identically to the sum of responses shown in the second row, except for some minor differences mostly over the Atlantic and European sectors. This suggests that the response to the total heating field can be approximated by a simple linear summation of the responses to each regional heating field. Therefore, an examination of the response to convection in each regional domain can give insight as to which regions are responsible for the similarities and differences we see between the extratropical responses to ENSO-like and MJO-like convective heating.

For the El Niño case, we see that the modeled height response to convective forcing in domains 4, 5, and 6 is most similar to that in the total response over the North

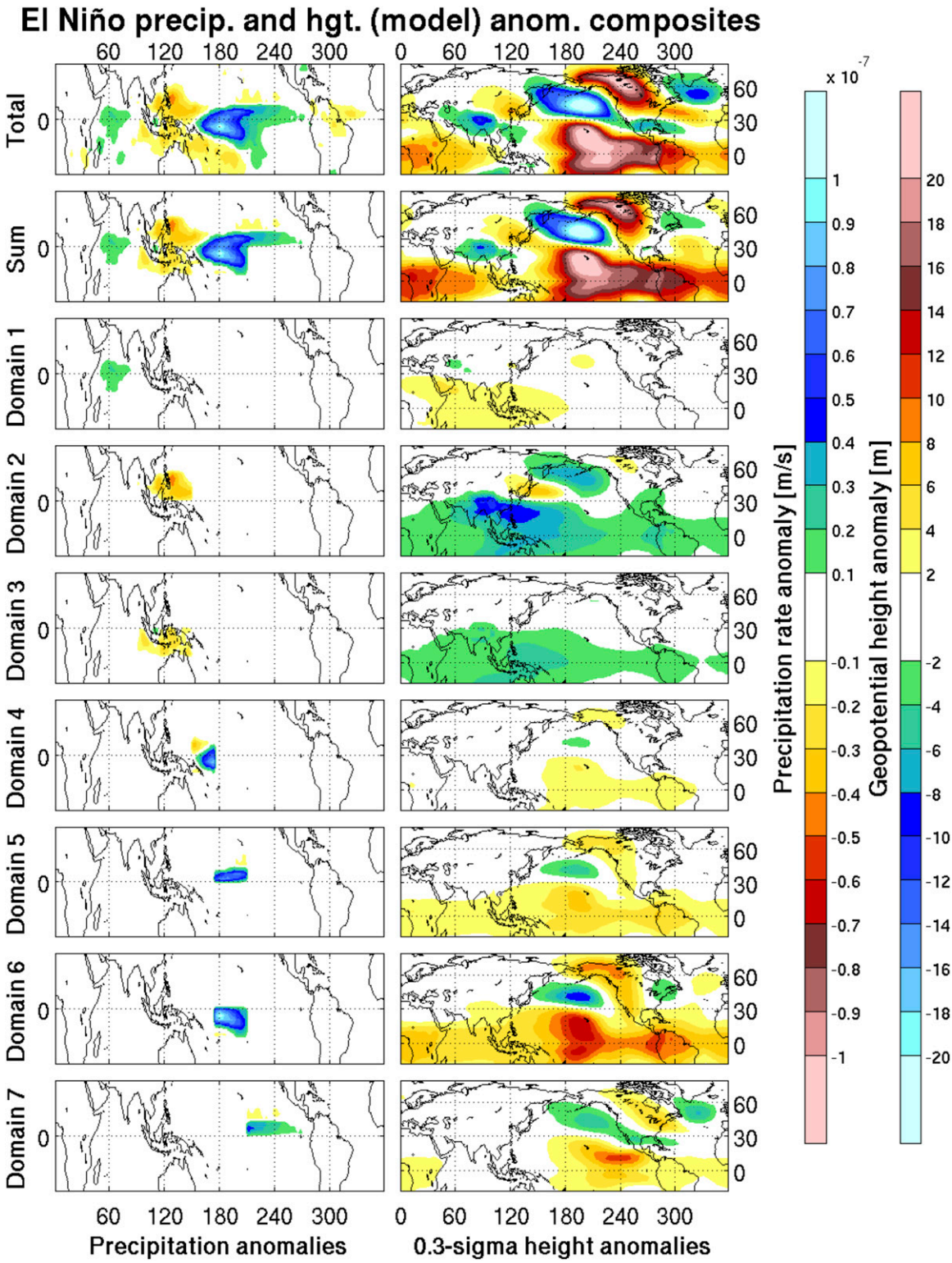

FIG. 3. (left) Precipitation composites used to generate the model El Niño heating field, and (right) the corresponding days-7–10 0.3σ geopotential height anomaly. (top) The model run forced with the full heating field (identical to Figs. 1a and 2a). (rows 3–9) The model run forced with a heating field restricted to domains 1–7, respectively (see Fig. 1a and text). (row 2) The sum of rows 3–9.

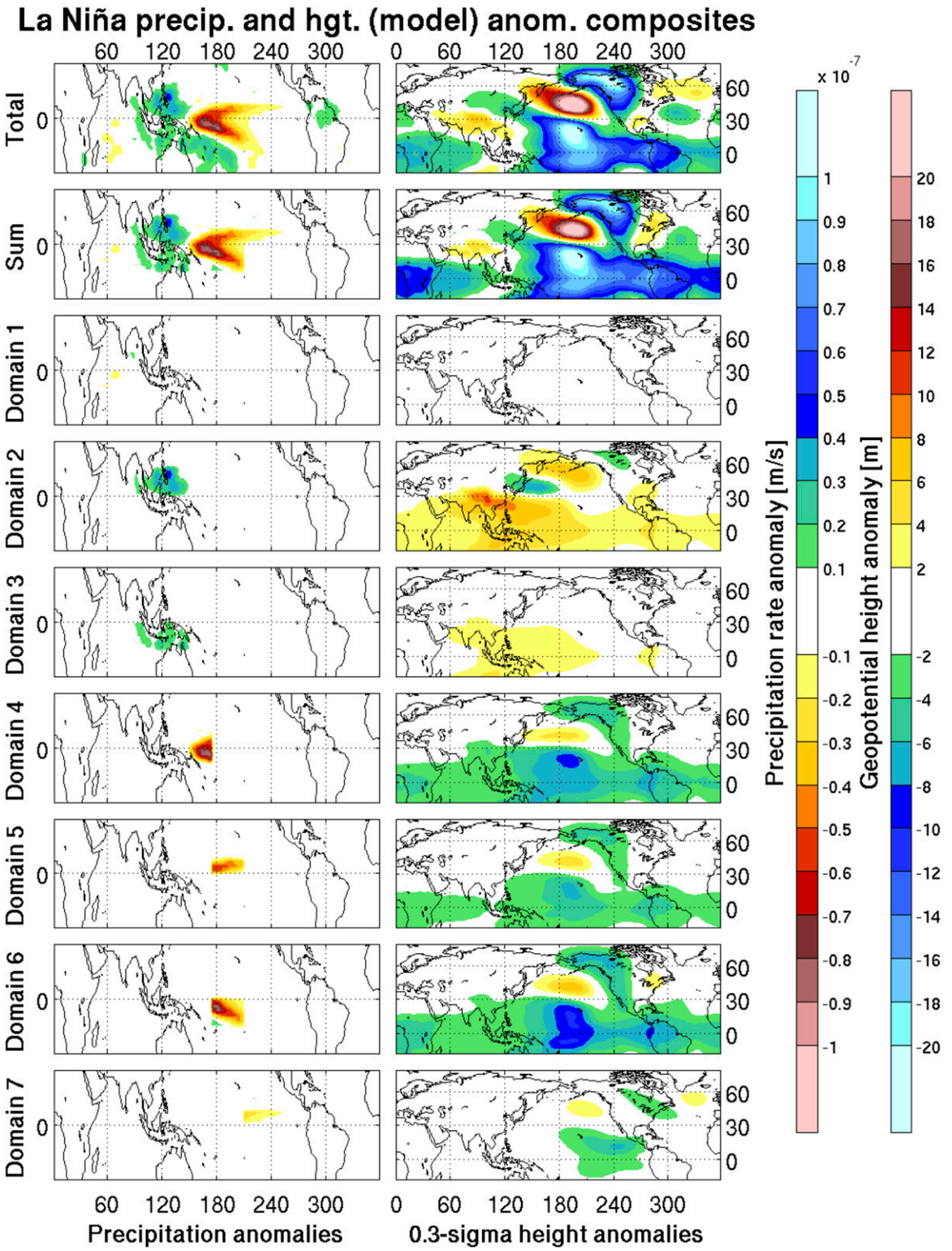

FIG. 4. As in Fig. 3, but for the La Niña case.

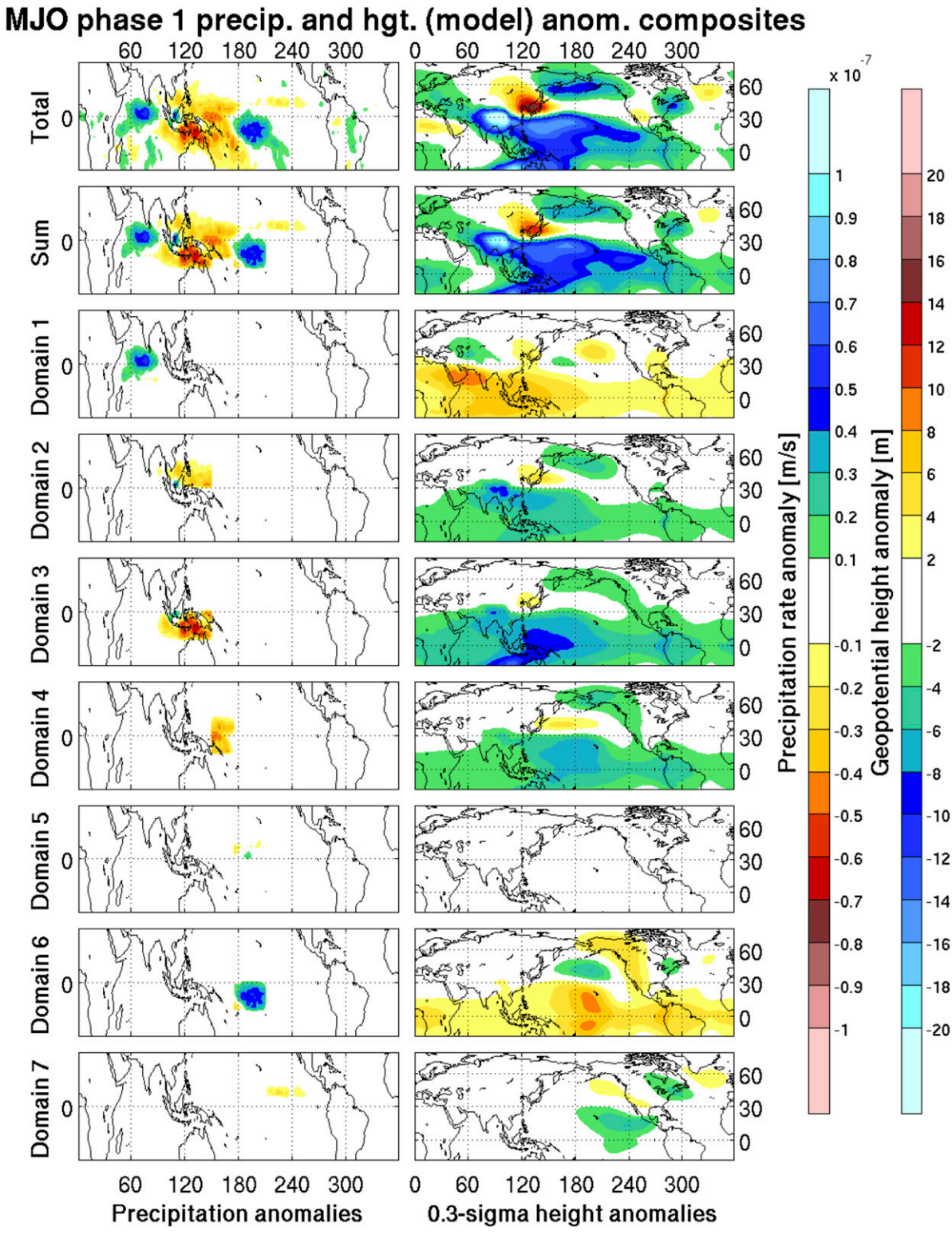

FIG. 5. As in Fig. 3, but for the MJO phase 1 case.

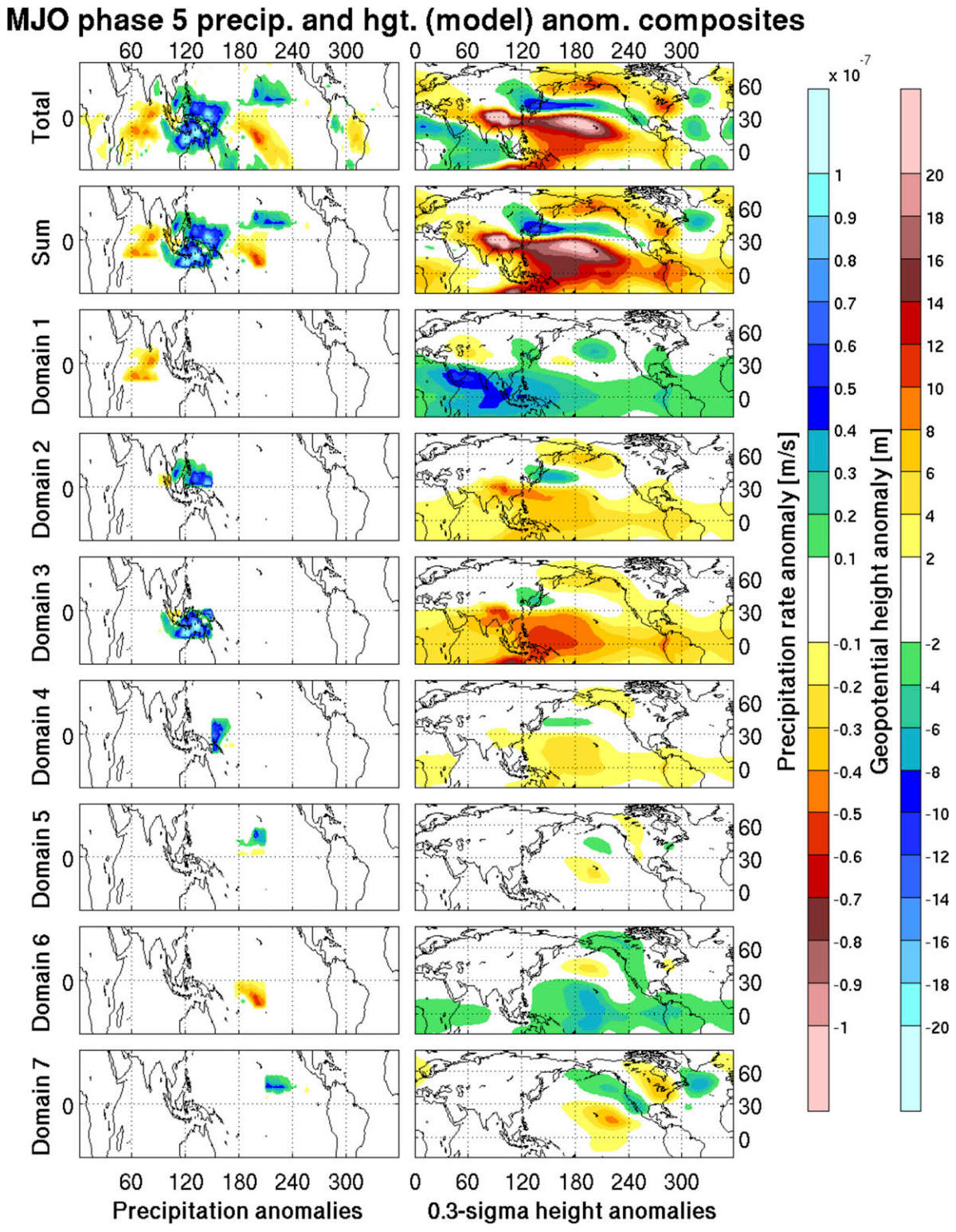

FIG. 6. As in Fig. 3, but for the MJO phase 5 case.

Pacific and North America, with the latter of those domains having the strongest-amplitude signal (Fig. 3). The response to convective forcing in domains 2 and 3 shows opposite-signed anomalies over the tropical Pacific, although domain 2 does appear to be responsible for some of the negative anomaly signal seen near the Aleutian Islands. Convection in domain 7 is partially responsible for the negative anomaly south of Greenland. Figure 4 is the analogous figure for the La Niña case, where anomalies of opposite sign to those for El Niño can be seen. One difference between these two cases is evident in domain 4, where the El Niño convective signal contains anomalies of both signs, resulting in a weaker extratropical response compared to that for La Niña. The presence of a single-signed negative convective anomaly for domain 4 may be due to the convective threshold temperature being forced westward during La Niña (Johnson and Kosaka 2016). Therefore, the extratropical response to La Niña is almost equally partitioned between domains 4, 5, and 6.

The convective forcing and modeled response to individual domains for the MJO phase 1 case is shown in Fig. 5. Unlike the ENSO cases, the response to convective forcing in domains 2, 3, and 4 dominates the total extratropical response over the North Pacific and North America. Domain 3, the domain located over the Maritime Continent south of the equator, shows the largest-amplitude response. This is consistent with the fact that domain 3 also shows the largest-amplitude convective signal. Figure 6 is analogous to Fig. 5, but for the MJO phase 5 case. We see that Figs. 5 and 6 are almost exactly analogous, merely showing anomalies of opposite sign.

Several broader points can also be seen in Figs. 3–6. First, the region of the strongest convective anomalies (domains 2, 3, and 4 for the MJO cases and domains 4, 5, and 6 for the ENSO cases) tends to dominate the extratropical response. Second, we can see that, for each convective domain, precipitation anomalies of the same sign are followed by a same-signed response in the extratropics; for example, for the MJO phase 1 case, the response to domain 6 (which has a convective signal of the same sign as that of the corresponding El Niño case) looks like a weak version of that for El Niño. Third, there appears to be some cancellation between the response to warm pool convection and the response to central Pacific convection for each of the MJO and ENSO cases. An example of this can be clearly seen in the MJO cases in Figs. 5 and 6, where domain 6 actually gives an extratropical response that is opposite in sign compared with the domains 2 and 3. Finally, we see that the response to Indian Ocean convection does not appear to be overly important for the MJO and ENSO composites we examined. The results in Figs. 3–6 suggest, then, that even though the large-scale convective patterns associated with ENSO and the MJO show a similar spatial structure, the significant differences between the extratropical responses to ENSO-like and MJO-like forcing arise from the differences in the location and amplitude of the convective anomalies.

4. Observational results

We perform a similar set of calculations, as described in section 2, with the observational dataset. Specifically, Figs. 7–10 are analogous to Figs. 3–6 presented in section 3, with the following differences. First, the precipitation composites for domains 1–7 in the left column of each figure are based on analog days, as described in section 2, chosen such that the composite of the analogs closely matches the anomalous values inside the domain and zero outside of the domain. We see that the analog precipitation composites in the left column of Figs. 7–10 match well with the localized precipitation fields used to force the model runs (Figs. 3–6) and, notably, are near zero outside of the respective domains. The sum of the seven precipitation composites is shown in the second row of the left column. Second, the right column for domains 1–7 shows 300-hPa geopotential height anomaly composites for 7–10 days after those days that are used in the corresponding precipitation composites, representing the extratropical response to the corresponding anomalous tropical convection. For the right column of Figs. 7–10, statistical significance at each grid point is calculated using a Monte Carlo simulation as described in section 2 and is marked at the $p < 0.05$ level with stipples. In all four cases, we find that regions of statistical significance tend to align with regions of greater 300-hPa height anomalies in the extratropics (smaller-amplitude 300-hPa height anomalies are found to be statistically significant closer to the equator, as one would expect based on the smaller variance in that region).

First, we investigate the El Niño case in the observations. The results, which are shown in Fig. 7, are analogous to the model results seen in Fig. 3. The 300-hPa anomalous geopotential height composite associated with the total convective precipitation field is shown in the right column (first row), where we see that the extratropical response to El Niño–like convective anomalies corresponds to highs centered over central Asia, near Hawaii, over Canada, and over the Mediterranean Sea, with lows centered over southeastern Asia, the Gulf of Alaska, the southern United States, and along the west coast of northern Africa. All of these anomalies correspond very well with the sum of the composites for individual domains (right column, second row), as was

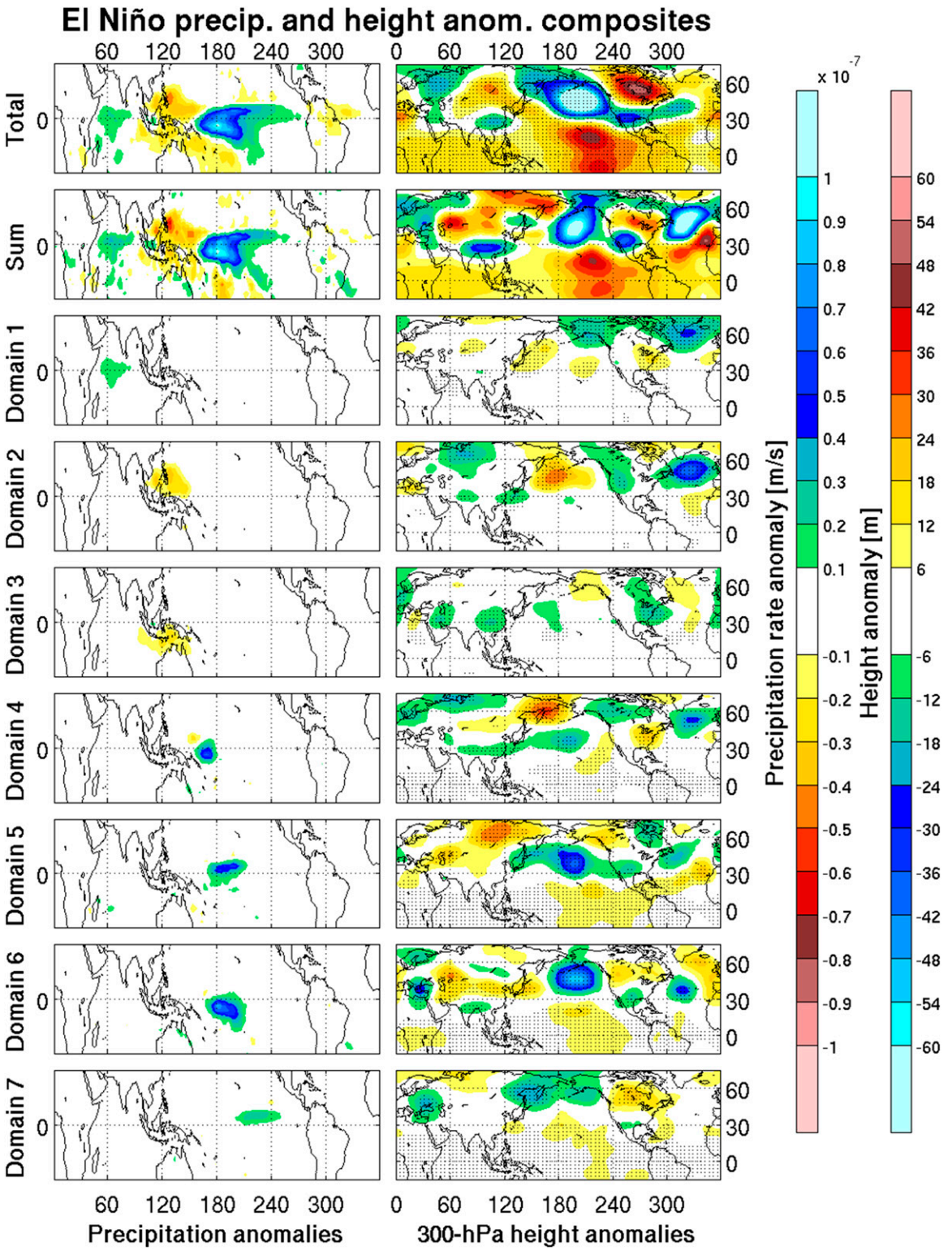

FIG. 7. (left) Observed El Niño precipitation composites based on analog days, and (right) the corresponding days-7–10 300-hPa geopotential height anomaly composites. (top) The full heating field case. (rows 3–9) Analog days for which the composite closely matches the precipitation anomalies only in domains 1–7, respectively (see text). (row 2) A sum of rows 3–9. In (right), stippling in rows 1 and 3–9 indicate regions where the anomalies are statistically significant at the $p < 0.05$ level.

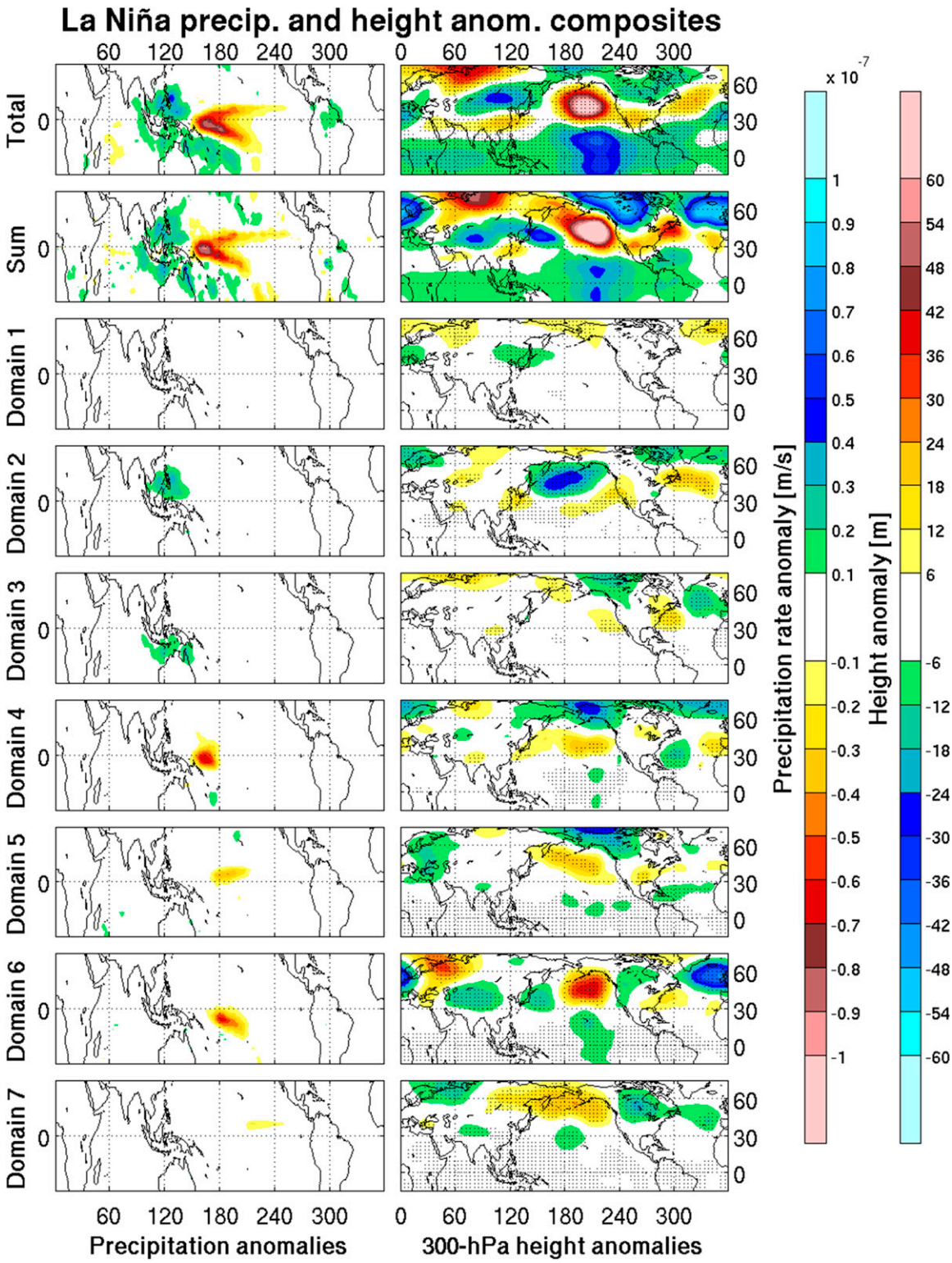

FIG. 8. As in Fig. 7, but for the La Niña case.

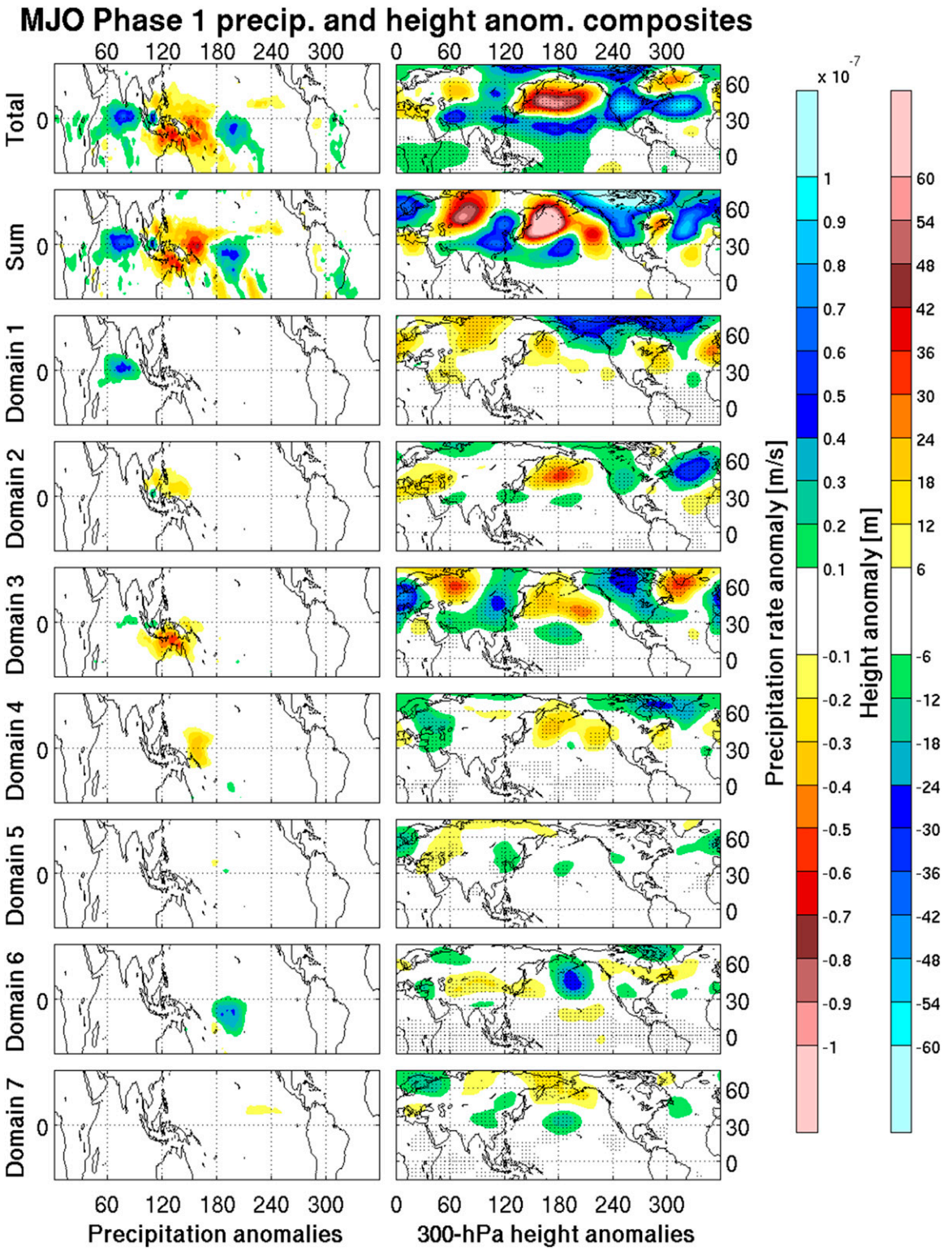

FIG. 9. As in Fig. 7, but for the MJO phase 1 case.

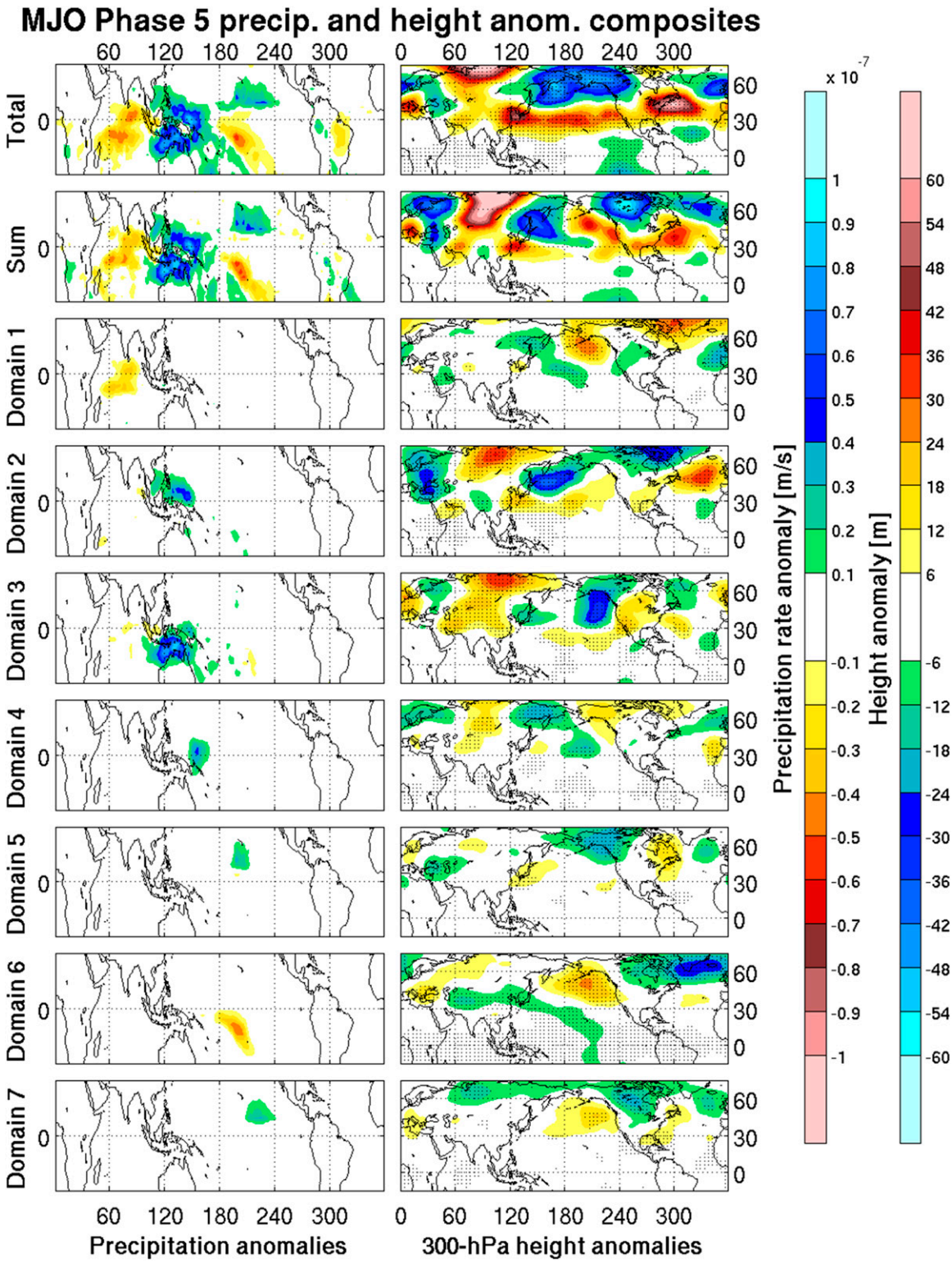

FIG. 10. As in Fig. 7, but for the MJO phase 5 case.

also the case in the modeled results seen in Fig. 3. Indeed, the pattern correlation over Asia, the North Pacific, and North America is 0.6918, significant at the $p < 0.01$ level. However, some differences are seen over the highest latitudes, especially over the North Atlantic sector. Some of these differences, especially those over the North Atlantic, may arise from the convective anomalies over South America, which are not included in the sum of the domains. The differences over the highest latitudes may be associated with nonlinear interactions between waves in midlatitudes. The overall match between the first and second rows allows us to investigate which convective domains are most responsible for the extratropical response. As with the model results in Fig. 3, we see that, in the observations, it is convective domains 5 and 6 over the central equatorial Pacific that contribute most to the response seen over the North Pacific and North America. In addition, it is seen that the extratropical response to the convective anomalies in domain 2, north of the equator over the Maritime Continent, partially cancels the contributions from domains 5 and 6.

The corresponding La Niña case is shown in Fig. 8. We see that the extratropical response shows largely the same spatial pattern as in the El Niño case, but with anomalies of opposite sign. Although there is a weak negative geopotential height anomaly in the El Niño case over northwestern Russia, the positive geopotential height anomaly in the La Niña case over the same region is spatially larger. Additionally, there is a negative geopotential height anomaly centered over the Beaufort Sea in the La Niña case. As in Fig. 7, we see that the sum of the responses to the individual convective domains in the second row matches very well with the response to the full La Niña–like convective composite. The worst match again appears to be over the North Atlantic sector, which may be associated with the convective anomalies over South America. The match over the highest latitudes is actually much better in the La Niña case than it is for El Niño. The pattern correlation over Asia, the North Pacific, and North America, between the first and second row of the right column, is very strong at 0.7941, which is significant well beyond the $p < 0.01$ level. Because the overall match is good, we can again investigate which domains are most responsible for the overall signal. We see that the anomalies over the North Pacific and North America match best with the responses to domains 4, 5, and 6. Unlike the El Niño case, and as in the model results, the precipitation anomalies in domain 4 are very strong and are of one sign for La Niña (perhaps related to sensitivity to the convective threshold SST). Therefore, domain 4 appears to be more important in La Niña than it is in El Niño. This difference also helps to explain the more prominent anomaly over northwestern Russia, as domain 4 is seen to substantially impact that region. The cancellation from domain 2 seen in the El Niño case over the North Pacific is not as obvious in the La Niña case; instead, the anomalies associated with domain 2 are largely in quadrature with the total response.

Next, we investigate the MJO phase 1 case (Fig. 9). The total 300-hPa anomalous geopotential height composite again matches well with the sum of the analog-based composites for the individual domains, with a pattern correlation value over Asia, the North Pacific, and North America of 0.6389, which is significant at the $p < 0.01$ level, though larger differences are seen over the Atlantic and European regions. The geopotential height anomaly composite (right column) for the full MJO phase 1 convective composite (the first row) shows highs centered to the south of the Aleutian Islands, over Mexico and the Gulf of Mexico, near the Cape Verde Islands, over central Europe and the Mediterranean, and over southern Asia. Lows are seen to the west of Hawaii, from Alaska down toward the U.S. Rockies, and over the North Atlantic south of Greenland. The biggest differences between the total and sum composites are located over Eurasia and the western North Atlantic. Many of these differences may be associated with convective anomalies over South America and Africa that are not accounted for in the sum in the second row. Additionally, there is a large-amplitude high centered off the coast of California in the second row that is weaker and farther south in the first row, which appears to be associated with domain 4 and may be a result of nonlinearities in the extratropical response. We see that the signal over the North Pacific and North America is mostly associated with domains 2, 3, and 4, as in the MJO phase 1 model run, which corresponds to convective anomalies over the Maritime Continent and the western equatorial Pacific. There is some cancellation over the North Pacific from domain 6. Therefore, as with the model results, we see that the extratropical geopotential height response to separate western and central Pacific heating anomalies is similar for El Niño and MJO phase 1, with the extratropical response to the total convective heating anomalies being of opposite sign in key regions because of the larger-amplitude convection in the central Pacific for El Niño and the western Pacific for MJO phase 1.

Finally, the MJO phase 5 case is examined, as seen in Fig. 10. As with all three of the previous figures, the sum of the 300-hPa geopotential height composites (right column) in the second row matches very well with the total 300-hPa geopotential height composite seen in the first row, although differences can be seen over some

regions, such as the northeastern Pacific. Specifically, the pattern correlation over Asia, the North Pacific, and North America is 0.5531, which is found to be statistically significant at the $p < 0.01$ level. Although in many locations Figs. 9 and 10 show opposite-signed geopotential height anomaly responses in the full convective case (first row in both figures), there are some differences as well. In Fig. 10, we see lows centered over the eastern Mediterranean Sea, near Bangladesh, over Kamchatka up through the Beaufort Sea and the Gulf of Alaska, south of the Gulf of Tehuantapec, and in the subtropical North Atlantic. Highs are centered over Siberia, to the northeast of Taiwan, over eastern Canada and Hudson Bay, and over the Arabian Sea. Many of these anomalies are also seen in the sum of composites in row 2, but there are also differences, most notably over the North Pacific and North American sectors. Specifically, we see a positive anomaly from the eastern Aleutians down to California in the sum, and a negative anomaly is located over the Canadian Archipelago. These anomalies are not seen in the composite based on the total MJO phase 5 precipitation field. Some of these anomalies appear to be associated with domains 1, 6, and 7. The differences may also partially arise from the convective anomalies over Africa and South America, which appear to be generally stronger for MJO phase 5 than in any of the other cases investigated. There may also be nonlinearities in the extratropical response that account for some of the differences we see. Because the match over the North Pacific and North American sectors is not as strong, it is more difficult to draw conclusions about which convective domains are responsible for the extratropical response. However, for the regions that match up well, it appears that domains 2 and 3 make the most significant contribution, as in the MJO phase 1 case. Domain 6 does not appear to contribute to cancellation over the North Pacific as compared to the sum in the second row, although it does show opposite-signed anomalies compared to the total in the first row.

The same broader points discussed in the model results can also generally be seen in the observational results in Figs. 7–10. The region of strongest convective anomalies again dominates the extratropical response. Although not as clean as in the model calculations, precipitation anomalies of the same sign in each convective domain tend to be followed by a same-signed response in the extratropics. As with the model results, a clean example is seen in domain 6, where, for both the MJO phase 1 and El Niño (MJO phase 5 and La Niña) cases, the response over the North Pacific is the same sign. There still appears to be some cancellation for both the MJO and ENSO cases between the response to convective anomalies over the Maritime Continent and the response to convective anomalies over the central Pacific, as there was in the model results. Finally, we again see that the Indian Ocean convection does not appear to be responsible for driving the extratropical response to the MJO and ENSO in this study. Therefore, Figs. 7–10 support the conclusion in the model calculations that the significant differences between the extratropical responses to ENSO-like and MJO-like forcing arise largely because of differences in the location and amplitude of the convective anomalies, although notably for MJO phase 5, as discussed previously, there may be other important factors to consider.

Because all ENSO states are represented in the MJO precipitation composites, there is a question of how much of the MJO signal is merely a consequence of a favored ENSO state. To test the impact of ENSO on the MJO analysis, we perform the analysis for Figs. 9 and 10 again, based on MJO precipitation composites for MJO days during only El Niño, neutral, or La Niña months. The results for the El Niño case are shown in Figs. 11 and 12 , for the neutral case in Figs. 13 and 14 , and for the La Niña case in Figs. 15 and 16 for MJO phases 1 and 5, respectively. We see for the neutral composites that the precipitation and 300-hPa geopotential height results match well with those in Figs. 9 and 10 (nearly identical amplitude and spatial structure, with statistical significance in similar locations), which suggests that any effect of El Niño days in the MJO composites in our original analysis is largely cancelled out by the effect of La Niña days in the same composites.

We next compare the MJO phase 1 precipitation and 300-hPa geopotential height anomalies for El Niño and La Niña to those for neutral ENSO. For MJO phase 1/El Niño, since the MJO phase 1/neutral ENSO (Fig. 13) and El Niño (Fig. 7) precipitation anomalies occur at about the same locations with the same signs, as expected, the amplitudes of all three precipitation anomalies for MJO phase 1/El Niño (Fig. 11) are larger than those of MJO phase 1/neutral ENSO. However, in contrast to MJO phase 1/neutral ENSO, the location of the largest-amplitude precipitation anomaly occurs over the central Pacific, not the warm pool region. Consistent with our argument that the response to tropical heating is determined primarily by the sign and amplitude of the largest heating anomaly, since the sign of the central Pacific anomaly is opposite to that of the warm pool anomaly, we see that the response to the MJO phase 1/El Niño (Fig. 11) shows extratropical anomalies that are of opposite sign to those for MJO phase 1/neutral ENSO in the expected locations (those locations associated with the El Niño composites). For MJO phase 1/La Niña, because the precipitation anomalies for MJO phase 1/neutral ENSO (Fig. 13) are of opposite sign to

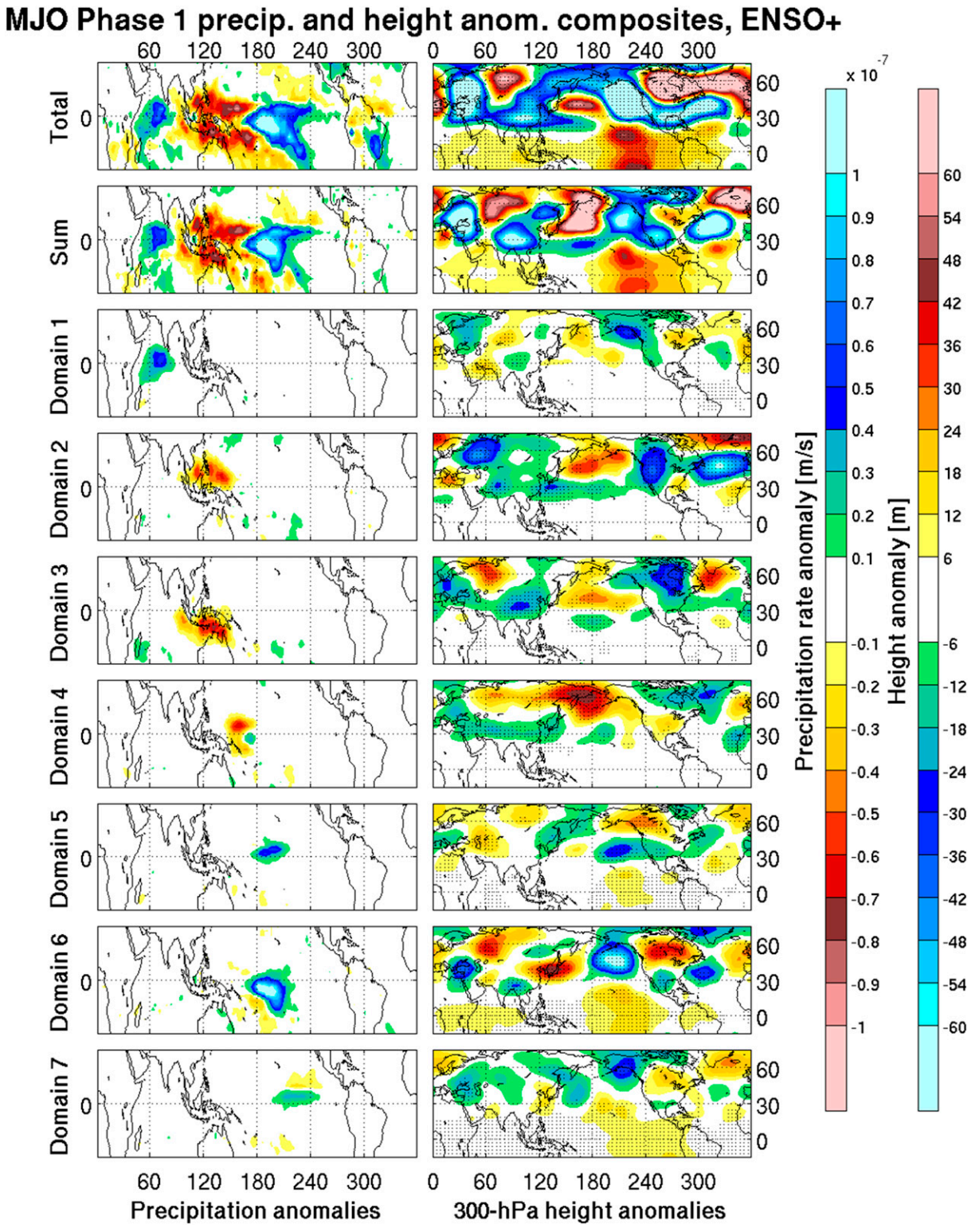

FIG. 11. As in Fig. 9, but using analogs from El Niño days.

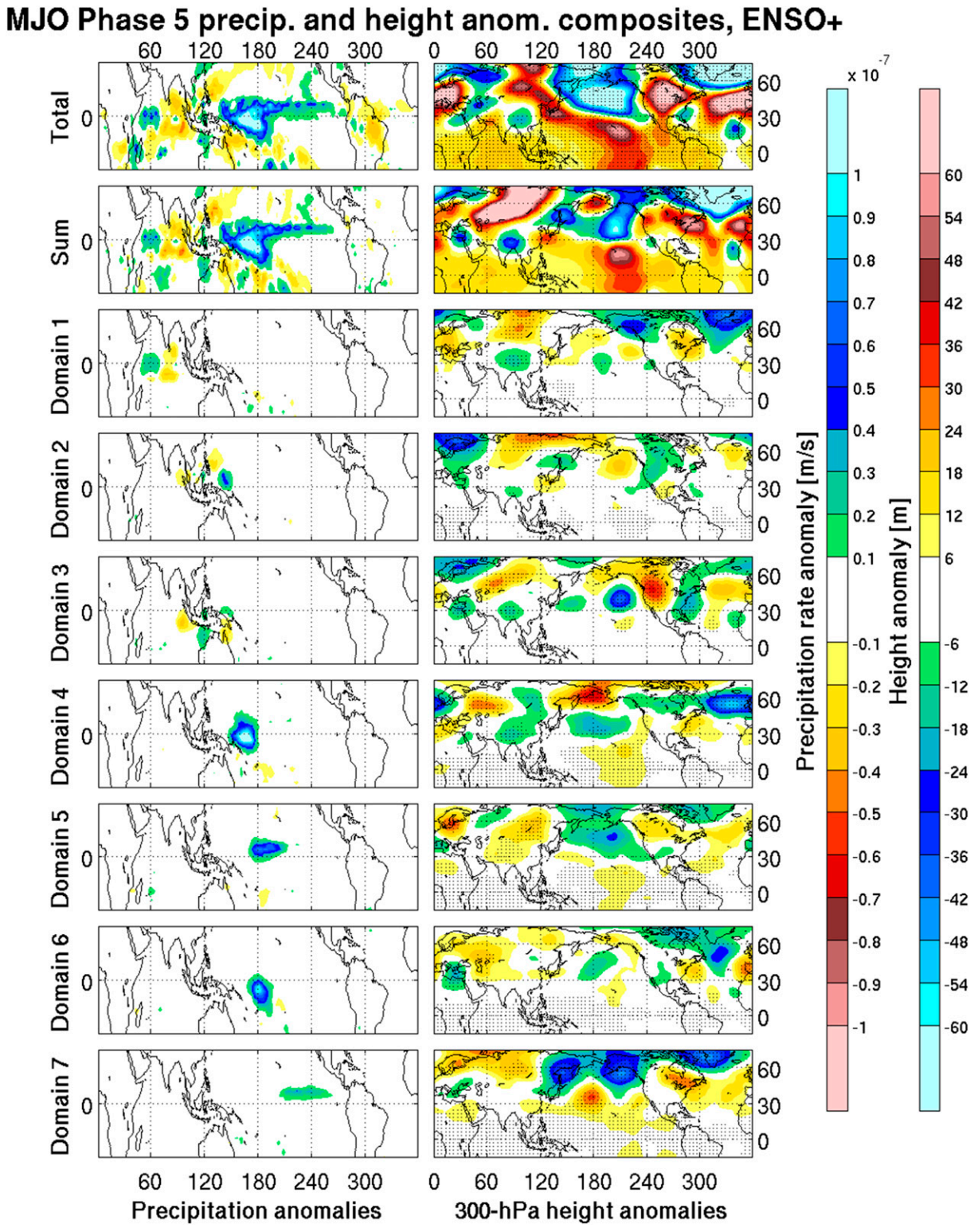

FIG. 12. As in Fig. 10, but using analogs from El Niño days.

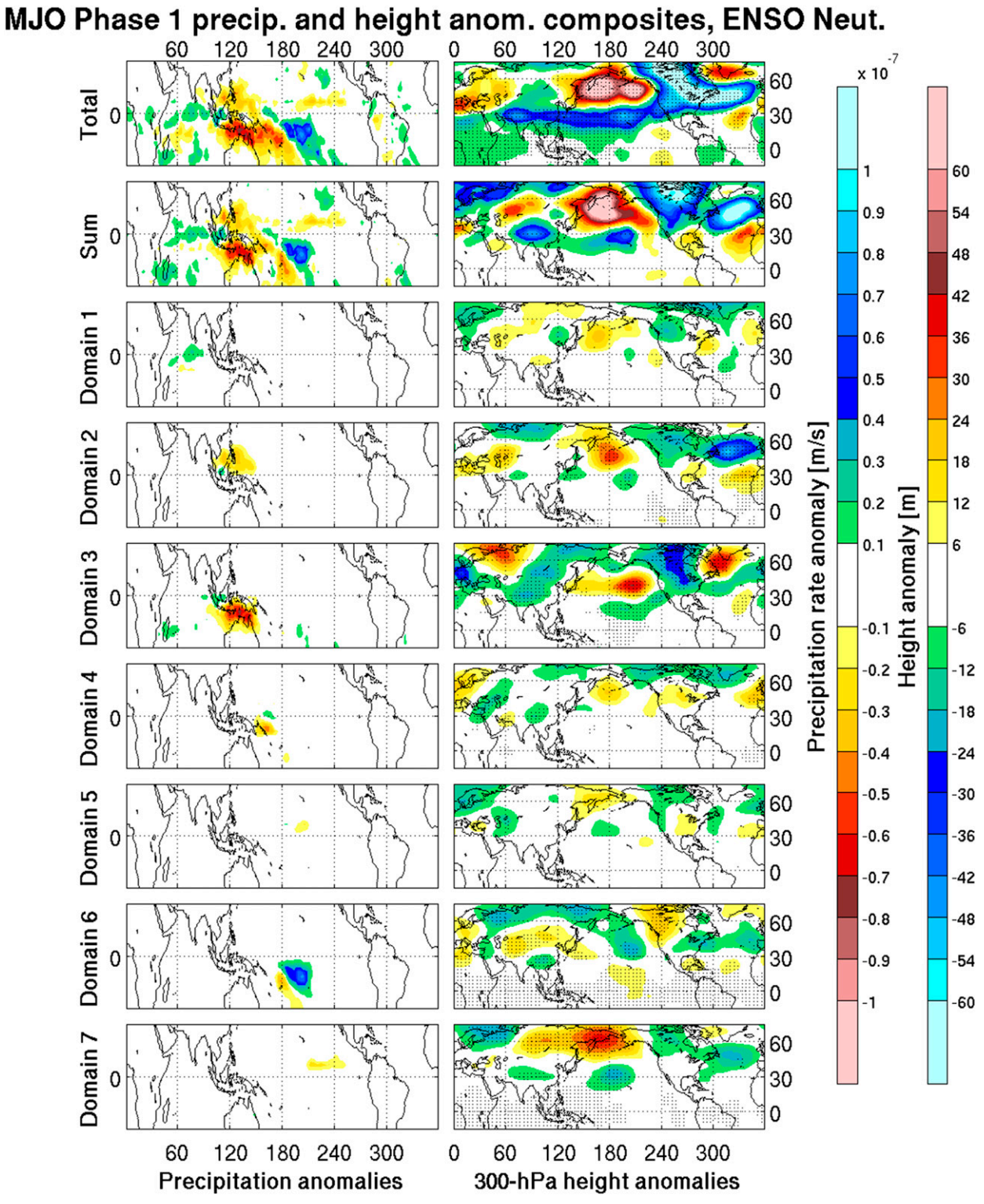

FIG. 13. As in Fig. 9, but using analogs from ENSO neutral days.

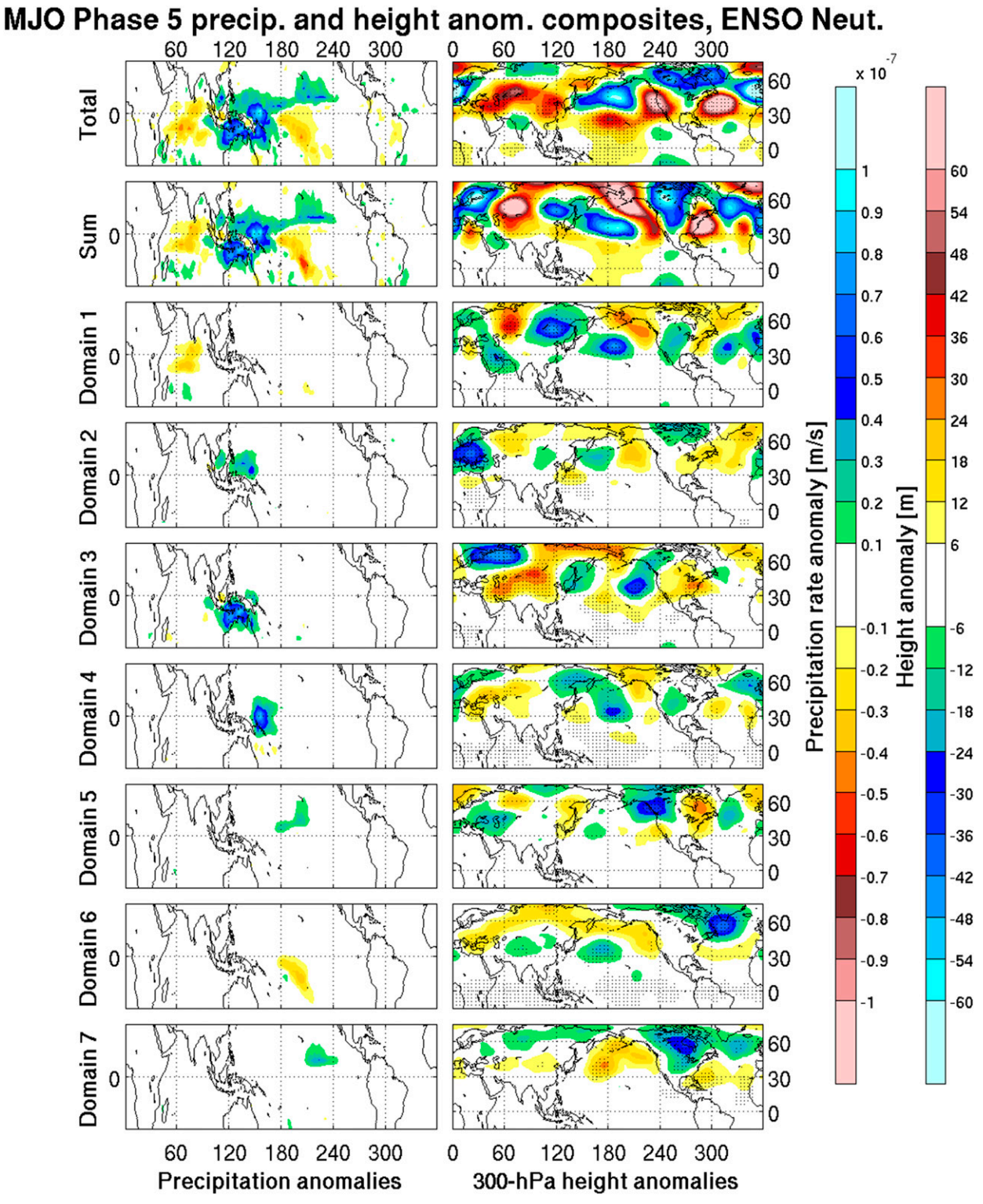

FIG. 14. As in Fig. 10, but using analogs from ENSO neutral days.

those for La Niña (Fig. 8), there is much cancellation between the MJO phase 1 and La Niña precipitation anomalies. For MJO phase 1/La Niña (Fig. 15), the central Pacific anomaly again dominates. Since this anomaly is of the same sign as the warm pool anomaly for MJO phase 1/neutral ENSO, the sign of the extratropical response over the northeastern Pacific and western North America is unchanged.

An examination of the MJO phase 5 precipitation and 300-hPa geopotential height anomalies shows features that are consistent with those for MJO phase 1, but with anomalies of opposite sign. For example, the signs of the MJO phase 5/La Niña and MJO phase 5/neutral precipitation anomalies are the same, and the largest MJO phase 5/La Niña precipitation anomaly is located over the central Pacific. Consistently, the signs of the MJO phase 5/La Niña 300-hPa (Fig. 16) geopotential height anomalies are opposite to that for MJO phase 5/neutral ENSO (Fig. 14). The MJO phase 5/El Niño precipitation anomalies are of the opposite sign as those for MJO phase 5/neutral ENSO. Again, since the largest precipitation anomaly is located over the central Pacific, the signs of the MJO phase 5/El Niño 300-hPa geopotential height anomalies (Fig. 12) are the same as those for MJO phase 5/neutral ENSO (Fig. 14).

5. Conclusions

In this study, we investigated the role of equatorial convective precipitation anomalies in forcing varied extratropical responses. Specifically, we tested questions related to 1) whether a simple dynamical model can reproduce the main differences in the extratropical response to forcing by MJO phase 1 and El Niño (MJO phase 5 and La Niña), 2) if specific convective regions in the model can explain the majority of the extratropical response to the MJO and ENSO convective heating, 3) if differences in the relative strength of convective anomalies in key regions can explain the different extratropical responses between MJO and ENSO, and 4) if the model results with respect to questions 2 and 3 can be sufficiently reproduced in an observational dataset.

With regard to question 1, we find that the modeled response to ENSO-like convective heating anomalies is indeed quite different from that for the broadly similar convective heating anomalies associated with the MJO. Specifically, whereas the modeled response to MJO phase 1 (phase 5) convective heating anomalies produces a negative (positive) height anomaly over northwestern North America and the northeastern United States and a positive (negative) height anomaly centered over the southwestern United States, for the very similar El Niño (La Niña) convective heating anomalies, the modeled response generally produces anomalies of the opposite sign over those regions. This is consistent with the differences seen in the observations.

For questions 2 and 3, the model results suggest that the extratropical response in each case is essentially the linear summation of the extratropical response to convective heating anomalies in each convective subdomain. Both the amplitude and location of the anomalies are found to be important. With regard to the extratropical response over the North Pacific and North America to the MJO convective heating anomalies, it is found that the largest contribution is from the convective anomalies found over the warm pool region. Conversely, for ENSO, most of the extratropical response over the North Pacific and North America is associated with convective anomalies located over the central equatorial Pacific. These two regions generally correspond with the strongest convective heating anomalies for each case. In fact, convective anomalies over the warm pool and over the central equatorial Pacific tend to force opposite-signed extratropical responses over the North Pacific and North America, indicating that there is some cancellation over those regions. We also found that the Indian Ocean convective anomalies, which are relatively weak, do not appear to play a large role in the overall extratropical response over the North Pacific and North America. Therefore, the differences in the modeled response to MJO-like and ENSO-like convective forcing can be explained by the differences in the relative location and amplitude of the convective anomalies associated with MJO and ENSO.

Finally, for question 4, we developed a technique to reproduce the model results in an observational dataset. We found that, as with the model results, the total extratropical response to tropical convection over the North Pacific and North America can generally be seen as the sum of the responses to tropical convection over each subdomain. The exception to this was with MJO phase 5, for which the summation did not match well with the extratropical response to the total convective field over the region of interest. However, the rest of the observational results corroborate well with the model results, suggesting that, to a large degree, the differences we see in the extratropical response to MJO-like and ENSO-like tropical convective heating in the atmosphere can be explained by the difference in the relative strength and location of the convective heating anomalies.

Understanding the sensitivity of the extratropical response to the location and amplitude of tropical convection is potentially important. Because no two ENSO or MJO events are identical, understanding how differences in tropical convection may impact the extratropical response has forecasting implications. However, more research into nonlinearities in the extratropical response to tropical

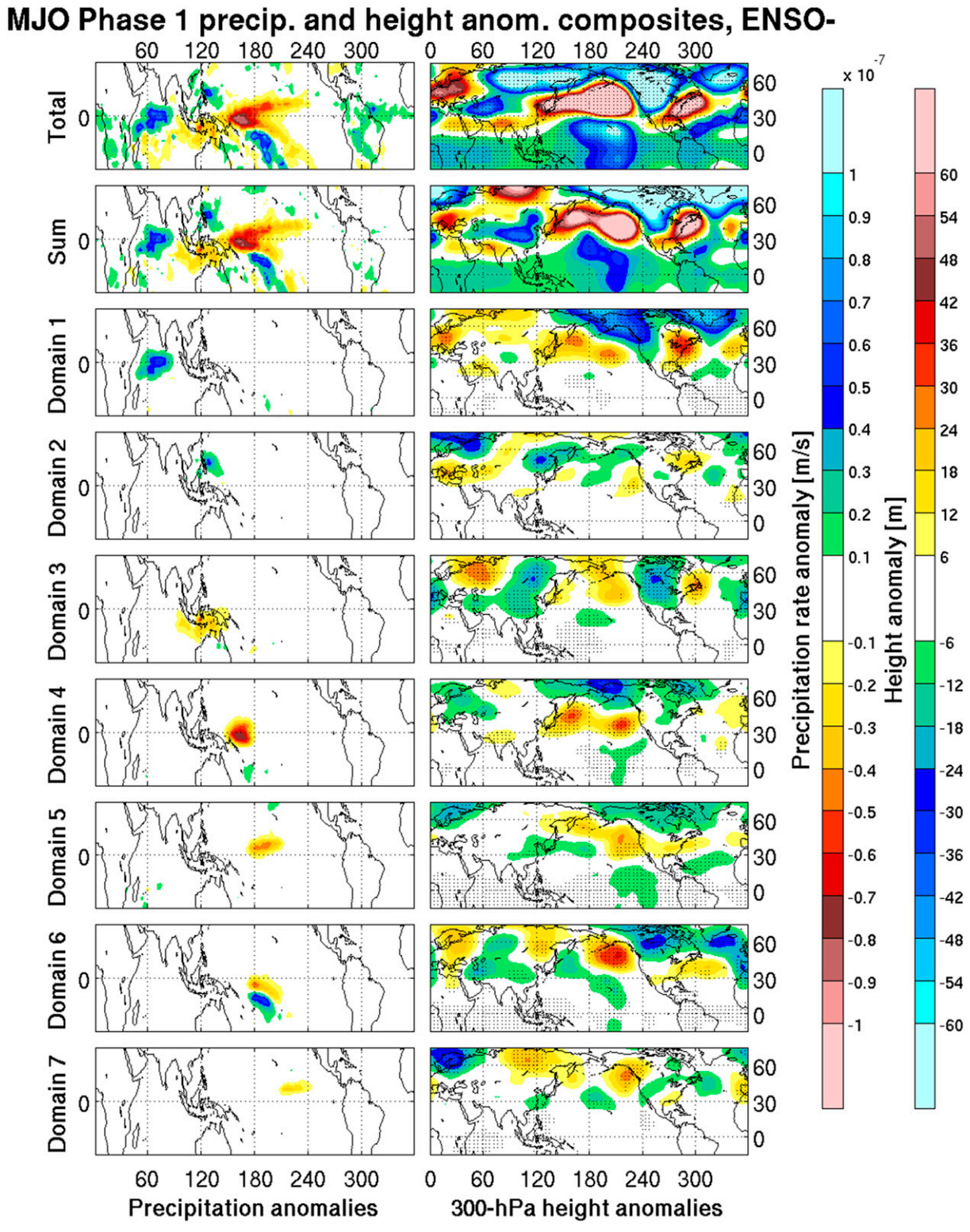

FIG. 15. As in Fig. 9, but using analogs from La Niña days.

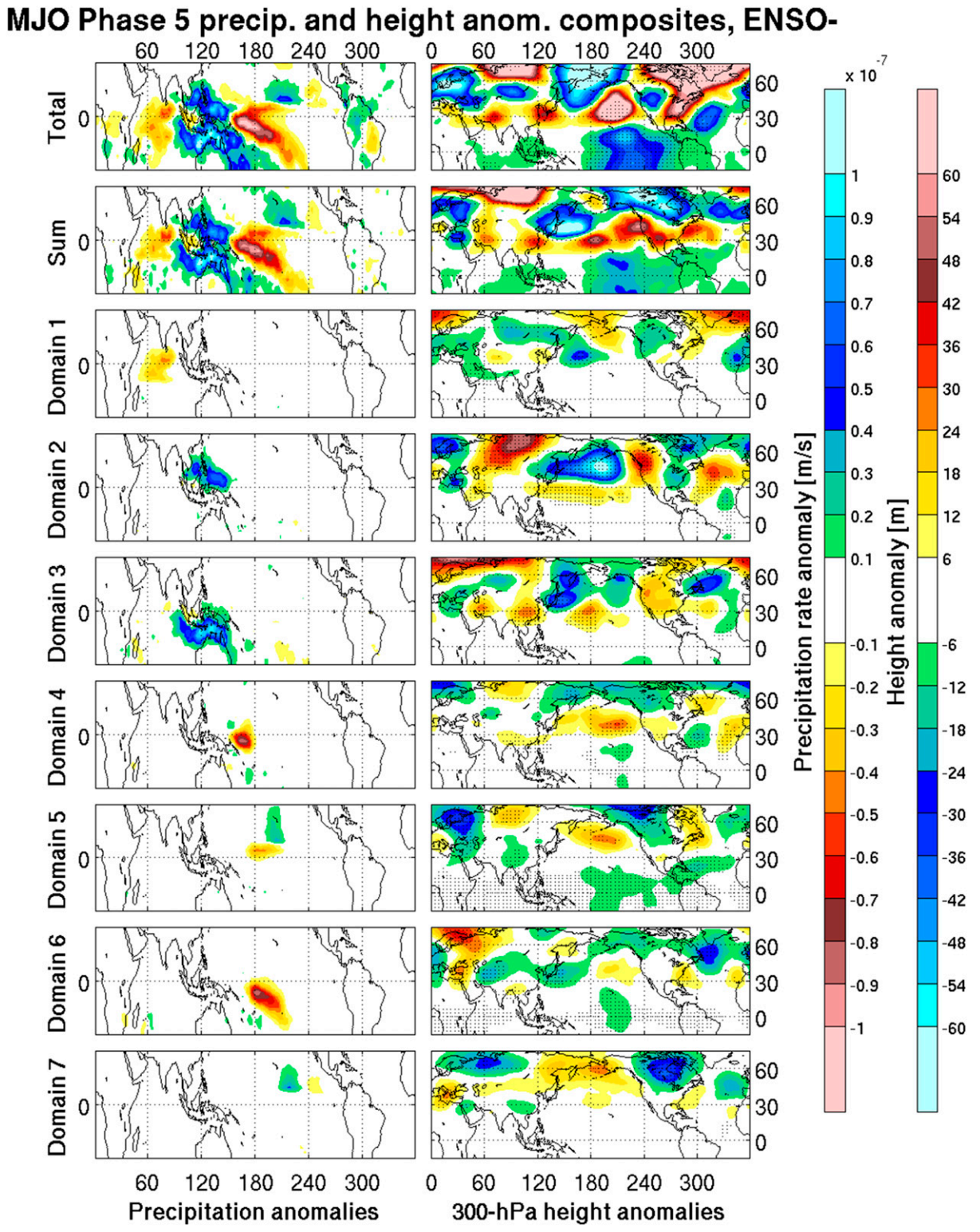

FIG. 16. As in Fig. 10, but using analogs from La Niña days.

convection, (as with the MJO phase 5 in the observational part of this study), as well as an investigation of other MJO phases, would further help to improve our understanding of the importance of tropical convection for the extratropical circulation.

Acknowledgments. This study is supported by National Science Foundation Grant AGS-1401220 and National Oceanic and Atmospheric Administration Grant NA14OAR4310190. We would also like to thank two anonymous reviewers, the European Centre for Medium-Range Weather Forecasts for providing us with the ERA-Interim data, and NOAA's Climate Prediction Center for providing the observed precipitation data.

REFERENCES

Bjerknes, J., 1966: A possible response of the atmospheric Hadley circulation to equatorial anomalies of ocean temperature. *Tellus*, **18**, 820–829, doi:10.1111/j.2153-3490.1966.tb00303.x.

——, 1969: Atmospheric teleconnections from the equatorial Pacific. *Mon. Wea. Rev.*, **97**, 163–172, doi:10.1175/1520-0493(1969)097<0163:ATFTEP>2.3.CO;2.

Dee, D. P., and Coauthors, 2011: The ERA-Interim reanalysis: Configuration and performance of the data assimilation system. *Quart. J. Roy. Meteor. Soc.*, **137**, 553–597, doi:10.1002/qj.828.

Franzke, C., S. B. Feldstein, and S. Lee, 2011: Synoptic analysis of the Pacific–North American teleconnection pattern. *Quart. J. Roy. Meteor. Soc.*, **137**, 329–346, doi:10.1002/qj.768.

Geisler, J. E., M. L. Blackmon, G. T. Bates, and S. Muñoz, 1985: Sensitivity of January climate response to the magnitude and position of equatorial Pacific sea surface temperature anomalies. *J. Atmos. Sci.*, **42**, 1037–1049, doi:10.1175/1520-0469(1985)042<1037:SOJCRT>2.0.CO;2.

Goss, M., and S. B. Feldstein, 2015: The impact of the initial flow on the extratropical response to Madden–Julian oscillation convective heating. *Mon. Wea. Rev.*, **143**, 1104–1121, doi:10.1175/MWR-D-14-00141.1.

Held, I. M., and M. J. Suarez, 1994: A proposal for the intercomparison of the dynamical cores of atmospheric general circulation models. *Bull. Amer. Meteor. Soc.*, **75**, 1825–1830, doi:10.1175/1520-0477(1994)075<1825:APFTIO>2.0.CO;2.

Horel, J. D., and J. M. Wallace, 1981: Planetary-scale atmospheric phenomena associated with the Southern Oscillation. *Mon. Wea. Rev.*, **109**, 813–829, doi:10.1175/1520-0493(1981)109<0813:PSAPAW>2.0.CO;2.

Hoskins, B. J., and D. J. Karoly, 1981: The steady linear response of a spherical atmosphere to thermal and orographic forcing. *J. Atmos. Sci.*, **38**, 1179–1196, doi:10.1175/1520-0469(1981)038<1179:TSLROA>2.0.CO;2.

Johnson, N. C., and S. B. Feldstein, 2010: The continuum of North Pacific sea level pressure patterns: Intraseasonal, interannual, and interdecadal variability. *J. Climate*, **23**, 851–867, doi:10.1175/2009JCLI3099.1.

——, and Y. Kosaka, 2016: The impact of eastern equatorial Pacific convection on the diversity of boreal winter El Niño teleconnection patterns. *Climate Dyn.*, **47**, 3737–3765, doi:10.1007/s00382-016-3039-1.

Kiladis, G. N., and K. M. Weickmann, 1992: Circulation anomalies associated with tropical convection during northern winter. *Mon. Wea. Rev.*, **120**, 1900–1923, doi:10.1175/1520-0493(1992)120<1900:CAAWTC>2.0.CO;2.

Lau, K.-M., and T. J. Phillips, 1986: Coherent fluctuations of extratropical geopotential height and tropical convection in intraseasonal time scales. *J. Atmos. Sci.*, **43**, 1164–1181, doi:10.1175/1520-0469(1986)043<1164:CFOFGH>2.0.CO;2.

Lin, H., and J. Derome, 2004: Nonlinearity of the extratropical response to tropical forcing. *J. Climate*, **17**, 2597–2608, doi:10.1175/1520-0442(2004)017<2597:NOTERT>2.0.CO;2.

Moore, R. W., O. Martius, and T. Spengler, 2010: The modulation of the subtropical and extratropical atmosphere in the Pacific basin in response to the Madden–Julian oscillation. *Mon. Wea. Rev.*, **138**, 2761–2779, doi:10.1175/2010MWR3194.1.

Mori, M., and M. Watanabe, 2008: The growth and triggering mechanisms of the PNA: A MJO-PNA coherence. *J. Meteor. Soc. Japan*, **86**, 213–236, doi:10.2151/jmsj.86.213.

Qin, J., and W. A. Robinson, 1993: On the Rossby wave source and the steady linear response to tropical forcing. *J. Atmos. Sci.*, **50**, 1819–1823, doi:10.1175/1520-0469(1993)050<1819:OTRWSA>2.0.CO;2.

Rasmusson, E. M., and T. H. Carpenter, 1982: Variations in tropical sea surface temperature and surface wind fields associated with the Southern Oscillation/El Niño. *Mon. Wea. Rev.*, **110**, 354–384, doi:10.1175/1520-0493(1982)110<0354:VITSST>2.0.CO;2.

Riddle, E. E., M. B. Stoner, N. C. Johnson, M. L. L'Heureux, D. C. Collins, and S. B. Feldstein, 2013: The impact of the MJO on clusters of wintertime circulation anomalies over the North American region. *Climate Dyn.*, **40**, 1749–1766, doi:10.1007/s00382-012-1493-y.

Rowntree, P. R., 1972: The influence of tropical east Pacific Ocean temperatures on the atmosphere. *Quart. J. Roy. Meteor. Soc.*, **98**, 290–321, doi:10.1002/qj.49709841605.

Sardeshmukh, P. D., and B. J. Hoskins, 1988: The generation of global rotational flow by steady idealized tropical divergence. *J. Atmos. Sci.*, **45**, 1228–1251, doi:10.1175/1520-0469(1988)045<1228:TGOGRF>2.0.CO;2.

Shukla, J., and J. M. Wallace, 1983: Numerical simulation of the atmospheric response to equatorial Pacific sea surface temperature anomalies. *J. Atmos. Sci.*, **40**, 1613–1630, doi:10.1175/1520-0469(1983)040<1613:NSOTAR>2.0.CO;2.

Ting, M., and P. D. Sardeshmukh, 1993: Factors determining the extratropical response to equatorial diabatic heating anomalies. *J. Atmos. Sci.*, **50**, 907–918, doi:10.1175/1520-0469(1993)050<0907:FDTERT>2.0.CO;2.

Trenberth, K. E., G. W. Branstator, D. Karoly, A. Kumar, N.-C. Lau, and C. Ropelewski, 1998: Progress during TOGA in understanding and modeling global teleconnections associated with tropical sea surface temperatures. *J. Geophys. Res.*, **103**, 14 291–14 324, doi:10.1029/97JC01444.

Wallace, J. M., and D. S. Gutzler, 1981: Teleconnections in the geopotential height field during the Northern Hemisphere winter. *Mon. Wea. Rev.*, **109**, 784–812, doi:10.1175/1520-0493(1981)109<0784:TITGHF>2.0.CO;2.

Wheeler, M. C., and H. H. Hendon, 2004: An all-season real-time multivariate MJO index: Development of an index for monitoring and prediction. *Mon. Wea. Rev.*, **132**, 1917–1932, doi:10.1175/1520-0493(2004)132<1917:AARMMI>2.0.CO;2.

Xie, P., and P. A. Arkin, 1997: Global precipitation: A 17-year monthly analysis based on gauge observations, satellite estimates, and numerical model outputs. *Bull. Amer. Meteor. Soc.*, **78**, 2539–2558, doi:10.1175/1520-0477(1997)078<2539:GPAYMA>2.0.CO;2.

Yoo, C., S. Lee, and S. B. Feldstein, 2012: Arctic response to an MJO-like tropical heating in an idealized GCM. *J. Atmos. Sci.*, **69**, 2379–2393, doi:10.1175/JAS-D-11-0261.1.